Mechanics of Materials 147 (2020) 103413

Contents lists available at ScienceDirect

Mechanics of Materials

journal homepage: www.elsevier.com/locate/mechmat

Static and dynamic shear-compression response of additively manufactured Ti6Al4V specimens with embedded voids

R. Fadida[a,b,*], A. Shirizly[a], D. Rittel[b]

[a] Rafael, POB 2250, Haifa 3102102, Israel
[b] Faculty of Mechanical Engineering, Technion, Haifa 3200003, Israel

ARTICLE INFO

Keywords:
Additive manufacturing
Laser powder bed fusion
Ti6Al4V
Artificial porosity
Static
Dynamic
Shear compression
Shear tension

ABSTRACT

The shear-compression response of additively manufactured Ti6Al4V specimens containing discrete artificial voids is investigated under quasi-static and dynamic loadings. Specimens containing spherical voids are designed with one or three voids with variable spacing between them. Specimens containing spheroidal prolate voids are designed with different void orientations with respect to the shear direction, while the total volume fraction of all void configurations is kept constant in the whole study. It is found that the presence of the void(s) reduces the displacement to failure, compared to the dense specimens, in both quasi-static and dynamic regimes. The shape and the number of voids have a noticeable effect on results only in the quasi-static regime. However, changing the distance between the spherical voids or changing the orientation of the prolate voids does not affect significantly the load-displacement curves in both strain rate regimes. Fractographic observations show that shear-compression specimens fail dominantly by shear, whereas previously investigated shear-tension specimens fail dominantly by tension. These observations are supported by preliminary numerical simulations.

1. Introduction

Additive manufacturing (AM) allows for the fabrication of complex geometries that cannot be produced using conventional means (Milewski, 2017), topology optimization (Wang et al., 2016) and assembly-based design (Oh et al., 2018). Although metal AM is still considered relatively expensive and less suitable for large-scale production, the technology is developing rapidly and can be expected to be integrated with conventional industry. The powder bed fusion (PBF) is one of the most widely used processes of metal additive manufacturing (Townsend et al., 2016). During this fabrication process, powder layers are repeatedly melted by a laser or electron beam, according to the patterns of a sliced CAD model, until a fully dense part is eventually obtained. Additively manufactured Ti6Al4V alloy is known to have strength properties that are comparable or even superior to those of similar wrought material, although its ductility is slightly lower (Facchini et al., 2010). The superior strength is mainly due to the fine-grained microstructure of the laser-processed material (Vrancken et al., 2012). One of the interesting advantages of AM is that internal features, such as embedded voids (porosity), can be fabricated in any shape and pattern for almost any material type. In that respect, it was demonstrated that spherical voids down to a diameter of 300 μm can be embedded within Ti6Al4V specimens (Fadida et al., 2018). Similarly, penny-shaped voids with a diameter of 300 μm were fabricated inside 316L stainless steel samples (Wilson-Heid et al., 2018). Both studies point to a *critical void diameter* (with respect to the specimen diameter) above which mechanical properties, such as elongation to failure decrease significantly due to the presence of the artificial void. Other than with additive manufacturing technology, the creation of internal voids by conventional means is quite hard (or even impossible) to achieve. Experimental investigation of internal artificial voids was conducted by Hosokawa (Hosokawa et al., 2013) based on the work of Weck and Wilkinson (Weck and Wilkinson, 2008). Hosokawa et al. used 0.05 mm thick pure copper sheets in which an array of 60 μm diameter holes was laser-machined. A multi-layer stack, which contains the laser-machined sheets and hole-free sheets alternately, was bonded by heating and later machined into dog-bone tensile samples. Using continuous X-ray computed tomography, the macroscopic plastic strain at void coalescence was measured. As mentioned, by using additive manufacturing technology, internal voids can be fabricated in a relatively simpler way, although there is still a limit to the minimum void size that can be generated with this technology.

The mechanics of void-containing solids is very well established. The most popular model for analyzing plastic flow in porous materials is due to Gurson (Gurson, 1977), which was modified and extended over the years, see e.g. (Chu and Needleman, 1980; Tvergaard and

* Corresponding author.
E-mail address: fadidarafi@gmail.com (R. Fadida).

https://doi.org/10.1016/j.mechmat.2020.103413
Received 3 October 2019; Received in revised form 4 April 2020; Accepted 5 April 2020
Available online 13 May 2020
0167-6636/ © 2020 Elsevier Ltd. All rights reserved.

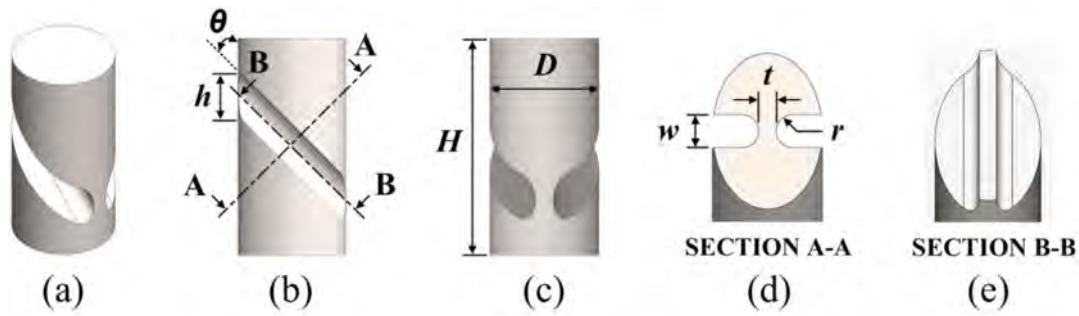

Fig. 1. A shear-compression specimen geometry: isometric projection (a), front view (b), side view (c), section view (A-A) perpendicular to the gauge inclination (d) and section view (B-B) parallel to the gauge inclination (e), which represents the mid-section of the gauge.

Table. 1
A. summary of the common geometrical dimensions of all SCS types.

Dimension	H	D	h	w	t	r	θ
Value [mm]	20	10	4.24	3	1.6	1.5	45°

Table. 2
Geometrical properties of all specimen types containing spherical void or voids.

Specimen type	Dense	Ø650	Ø450L2	Ø450L4
Number of artificial voids	*0*	*1*	*3*	*3*
Void diameter, d [μm]	-	*650*	*450*	*450*
Distance between voids, L [mm]	-	-	*2*	*4*
Void total volume [mm^3]	-	*0.143*	*0.143*	*0.143*
L / (d/2) ratio	-	-	*~9*	*~18*

Needleman, 1984). Gologanu et al. (Gologanu et al., 1993) extended the classical Gurson analysis to account for non-spherical voids. Nahshon and Hutchinson (Nahshon and Hutchinson, 2008) suggested an extension to Gurson model to account for damage growth in shear-dominated stress state. Until the advent of AM, an appropriate technology to fabricate embedded three-dimensional voids was not available and therefore, investigations were limited to mostly analytical and numerical studies. For example, the behavior of voids subjected to shear-dominated stress state was investigated numerically by several researchers (Dunand and Mohr, 2014; Nielsen et al., 2012; Scheyvaerts et al., 2011; Tvergaard, 2009). In-situ tomography experiments were recently conducted on as-received dual phase steel, exploring the nucleation and evolution of micro-voids under shear-dominated loading (Roth et al., 2018). However, similar experimental studies with controlled and embedded 3D voids, of variable size, spacing and shape, are less common in the literature. The mechanical response of void-containing specimens was investigated by Fadida et al. for compression (Fadida et al., 2015), for tension (Fadida et al., 2018) and recently for combined shear-tension (Fadida et al., 2019). Still, the subject of controlled (artificial) porosity under shear loading has not been studied thoroughly from an experimental standpoint, in both the quasi-static and dynamic loading regimes. The shear-compression specimen (SCS) of Rittel et al. (Rittel et al., 2002), later characterized extensively by Dorogoy and Rittel (Dorogoy and Rittel, 2005), enforces a shear-dominant stress state within the specimen's gauge section. Therefore it was found suitable for the present investigation of voids under combined shear-compression. The present study reports on the mechanical response of embedded spherical and spheroidal voids, in which a combined shear-compression stress state is imposed, at different strain rates. This paper is organized as follows. Section 2 describes the experimental technique and specimen design. Section 3 presents the experimental results. Section 4 shows the SEM fractographic analysis of the specimens, in which the characterization is extended to previously tested shear-tension specimens in order to establish a comparison. Section 5 describes the results of quasi-static numerical simulations for different void shapes (spherical vs. prolate) and different stress states (i.e., shear-compression vs. shear-tension). Section 6 discusses the experimental and numerical results, followed by summary and conclusions in Section 7.

2. Material and methods

2.1. Dynamic compression tests

The split Hopkinson pressure bar (SHPB) is a common tool for the mechanical characterization of materials at high rates of loading in the range of $10^2 - 10^4\ s^{-1}$. The experimental principles and apparatus were originally introduced by Kolsky (Kolsky, 1949) for compression. The technique has been modified over the years for loading in tension

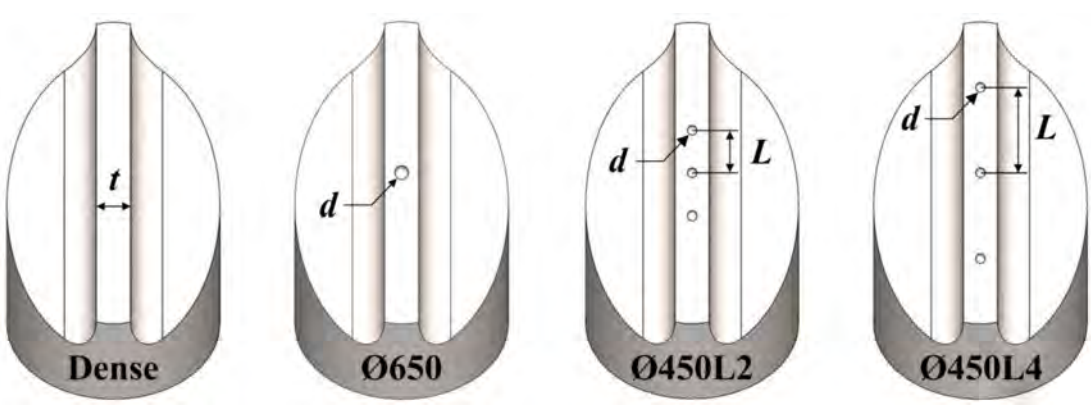

Fig. 2. A cross-section view of the specimen's gauge showing the spherical void arrangements in each specimen type. From left to right: Dense, Ø650, Ø450L2 and Ø450L4.

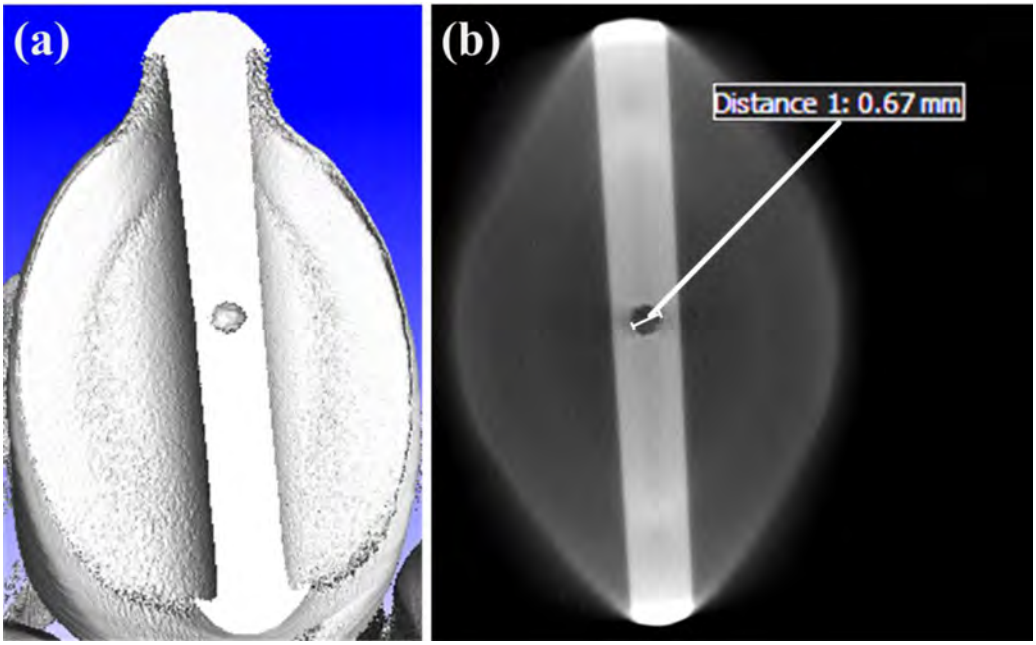

Fig. 3. A typical CT image of specimen that contains Ø650 μm void (a) and its measured diameter (b).

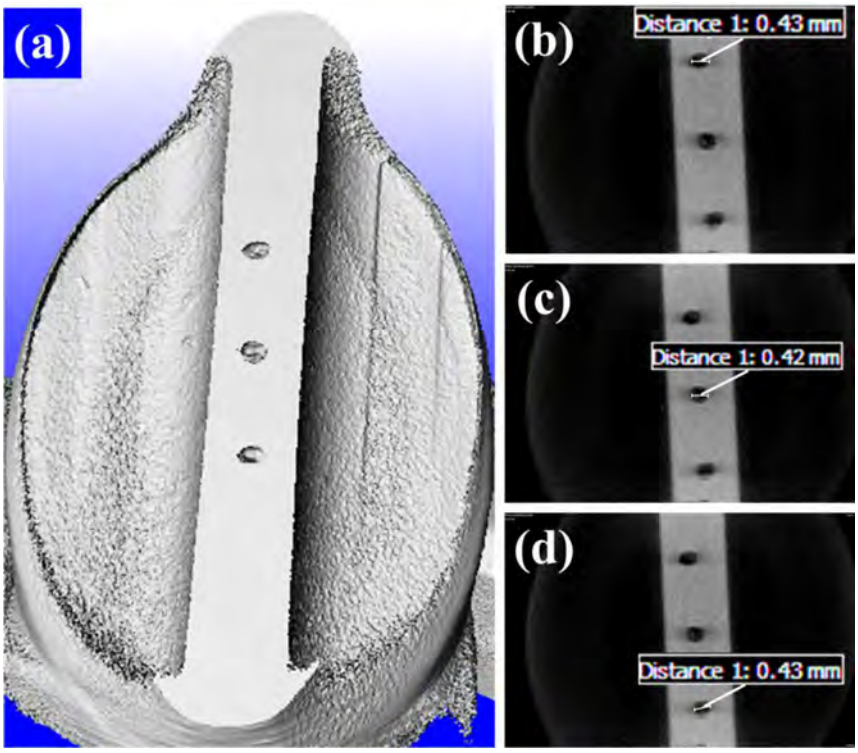

Fig. 4. A typical CT image of specimen that contains 3 × Ø450 μm voids (a) and its measured diameters (b-d).

(Harding et al., 1960) and torsion (Lewis and Campbell, 1972) and their combination. In the compression test, the cylindrical specimen is sandwiched between two long cylindrical bars, named as incident and transmitted bars, made of hardened C300 maraging steel on our setup. The compressive pulse is generated by shooting a cylindrical striker against the incident bar. The pulse propagates along the incident bar and when it reaches to the incident/specimen interface, part of it is being reflected back, while the other part, propagates through the specimen and continue to the transmitted bar. The measurement of the stress waves is done using strain gauges that are cemented at mid-length of the incident and transmitted bars. During the experiment, three strain pulses are measured, which are the incident, reflected and transmitted signals. According to the measured strains, the forces on both sides of the specimen are calculated and verified for dynamic equilibrium. If dynamic force equilibrium is obtained, then the resulting stress-strain curve is assumed to be valid. Further developments of the technique and theory can be found in many literature sources, see e.g., (Gray III GT, 2000).

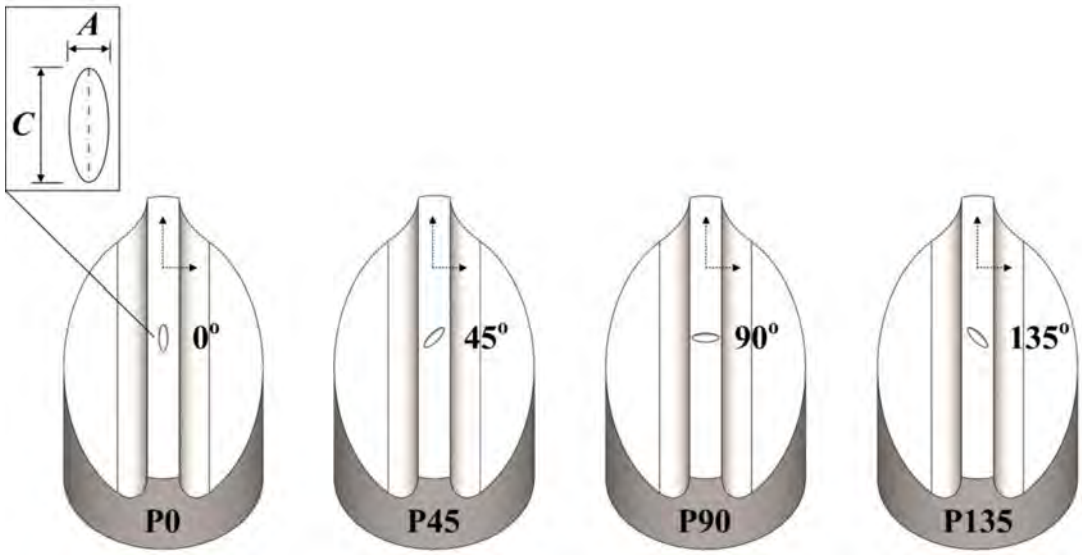

Fig. 5. A cross-section view of the specimen's gauge showing the prolate void orientation in each specimen type. From left to right: P0, P45, P90 and P135.

Table. 3
Geometrical properties of all specimen types containing prolate voids.

Specimen type	P0	P45	P90	P135
Number of artificial voids	1	1	1	1
Void short diameter, A [μm]	450	450	450	450
Void long diameter, C [μm]	1350	1350	1350	1350
Void orientation	0°	45°	90°	135°
Void total volume [mm^3]	0.143	0.143	0.143	0.143

2.2. Specimen design and manufacturing

2.2.1. Shear-compression specimen design

The shear-compression specimen (SCS) geometry consists of a cylinder, in which two identical semi-circular slots are machined at 45° with respect to the cylinder's axis of symmetry, forming a narrow gauge section. When the SCS is axially loaded the gauge section is subjected to a shear-dominated stress state. Rittel et al. (Rittel et al., 2002) showed from the very beginning of specimen development that the state of stress in the gauge is three-dimensional. However, the closest term to define the stress state in the gauge is sim*ple shear* combined with compression, rather than pur*e shear*. The reader may refer to (Butcher and Abedini, 2017) for a comprehensive discussion on the characterization of simple shear deformation. The CAD model of the SCS and cross-sectional views of the gauge are presented in Fig. 1.

2.2.2. Shear-compression specimen manufacturing

A series of fully dense cylindrical rods were additively manufactured by the laser-based powder bed fusion (L-PBF) process. To reduce the effect of residual stress due to the cyclic sequence of highly

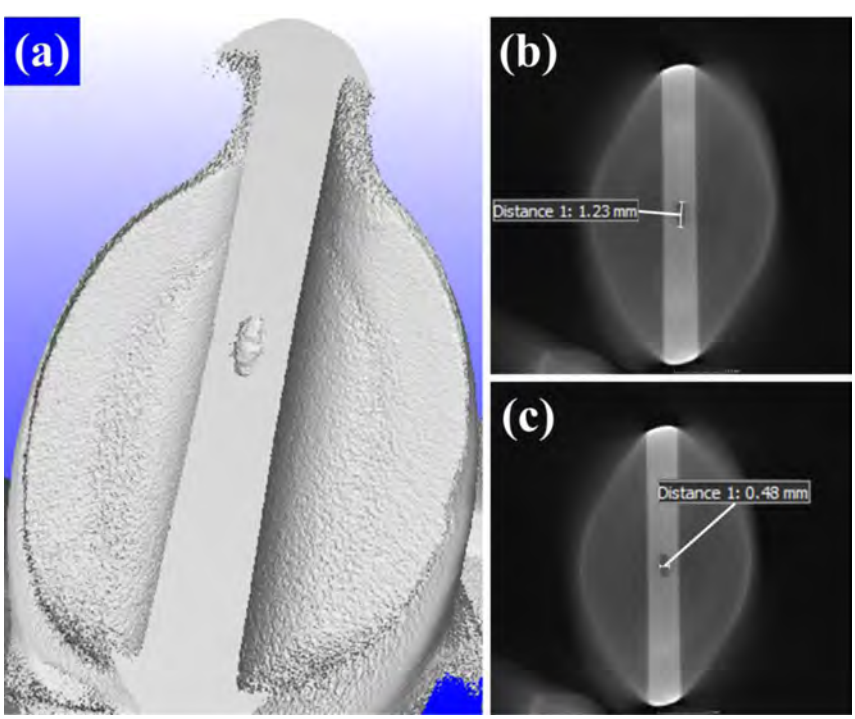

Fig. 6. A typical CT image of specimen that contains prolate void oriented by 0° (a) and its measured diameters (b-c).

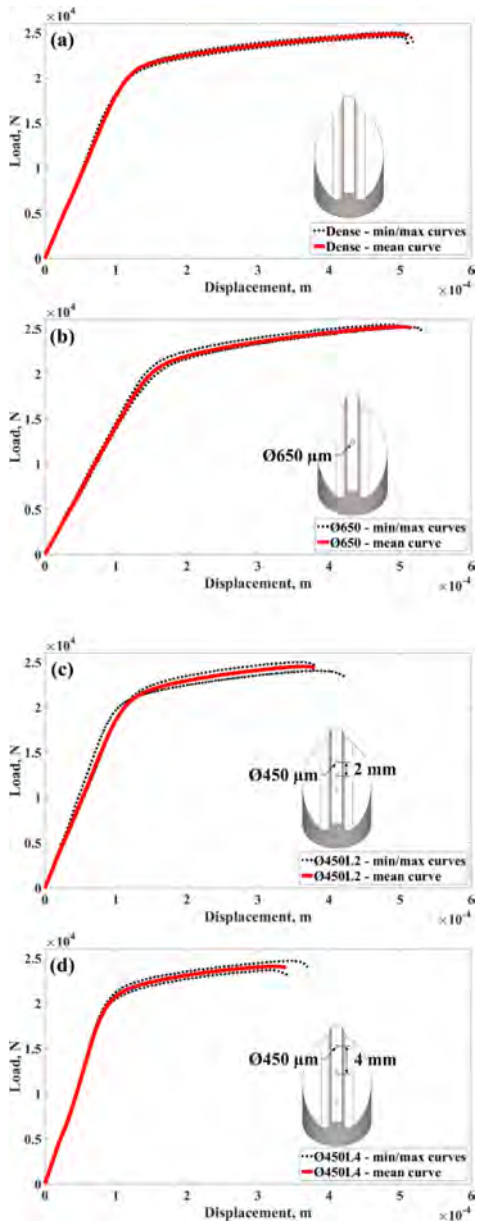

Fig. 7. Load-displacement curves of all specimens containing one spherical void or three voids (b-d), compared to dense specimens (a), at a nominal strain rate of $2.8 \times 10^{-3}\ s^{-1}$.

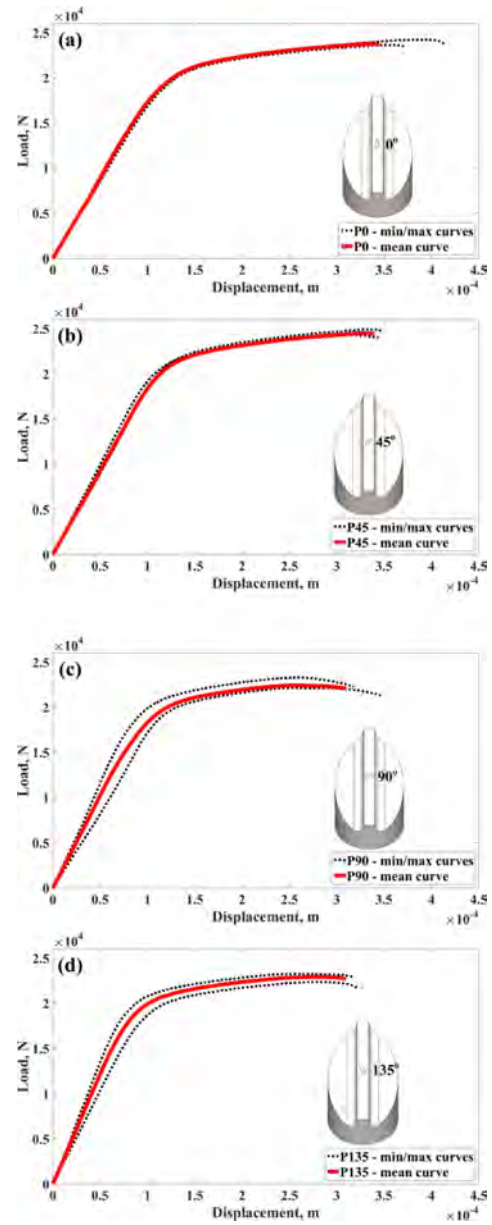

Fig. 8. Load-displacement curves of all specimens containing one prolate void at a nominal strain rate of $2.8 \times 10^{-3}\ s^{-1}$.

localized heating followed by rapid cooling, the rods were subjected to a stress relief process as follows: 650°C for 3h in vacuum environment. Then, they were machined (CNC milling) to the final geometry according to Fig. 1. No further machining was applied to the outer surface of the specimen. The geometry and dimensions of the specimen's gauge section, as shown in Table 1, based on Dorogoy et al. (Dorogoy et al., 2015). Manufacturing tolerances and a quality control examination were applied to ensure that specimens will be almost identical in dimensions. The typical tolerance for specimen's gauge section dimensions (Fig. 1 d) was of the order of ± 0.1 mm.

2.2.3. SCS with spherical voids

A series of void-containing specimens and fully-dense specimens (as a reference), were additively manufactured. The first specimen type contains single void, Ø650 µm in diameter (d) located at the gauge's geometric center. The second type contains three voids, Ø450 µm in diameter, located in a straight line along the gauge so that the spacing (L) between their centers is 2 mm. To allow for comparison, the volume of the single void within the first specimen type was designed to be equal to the total volume of the three voids within the second specimen type. The third type is similar to the second type but, the distance between the voids was set to 4 mm. In the specimens that contain three voids, the ratio of voids spacing to void radius is 9 and 18 respectively. Thus, no interaction effects between artificial voids are expected to be involved during the elastic-plastic deformation (Brown and Embury, 1973). Fig. 2 illustrates the voids arrangement inside the shear-compression specimens and Table 2 summarizes the geometric properties of the voids.

Figs. 3 and 4 show a computed tomography (CT) images of the specimen containing a single Ø650 µm void, and the other containing 3 × Ø450 µm voids with $L = 2$ mm, respectively. The CT scans show that the shape of the Ø650 µm void is nearly spherical, characterized by an inner jagged surface, while the shape of the Ø450 µm voids seems slightly less spherical. All measurements of spherical void diameter were kept within tolerance of ± 50 µm, compared to the model's

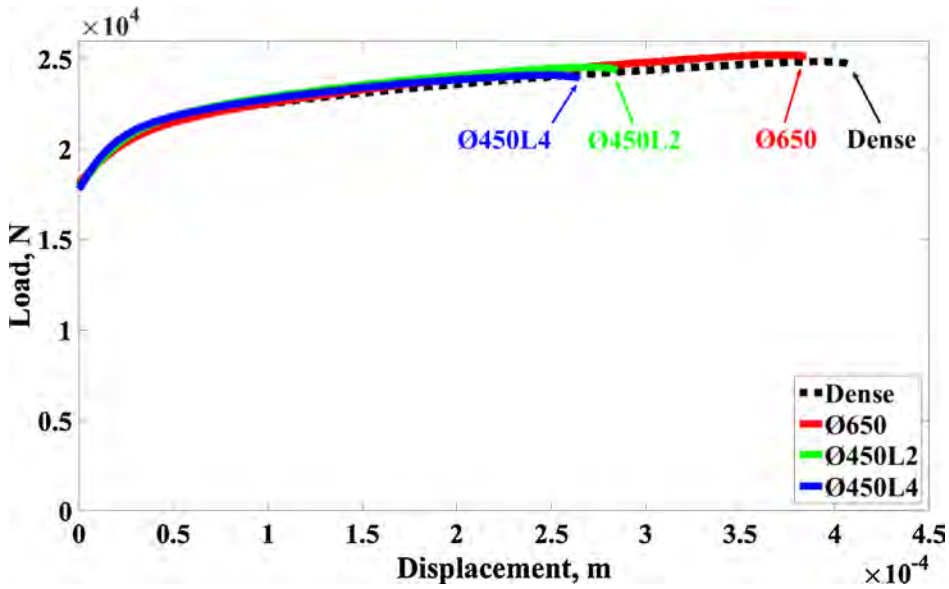

Fig. 9. Load-plastic displacement mean curves of all specimens containing one spherical void or three voids, compared to dense specimens, at nominal strain rate of $2.8 \times 10^{-3}\ s^{-1}$.

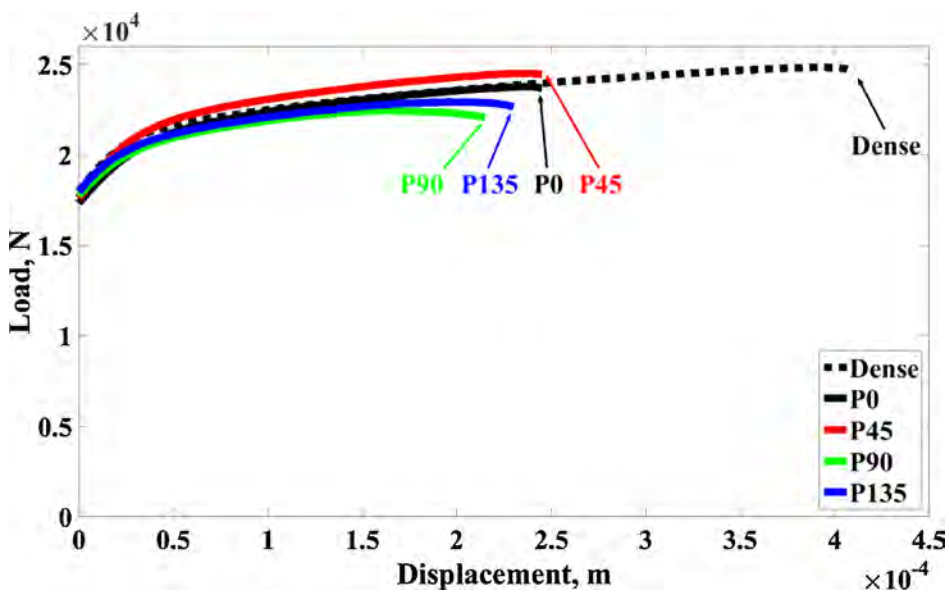

Fig. 10. Load-plastic displacement mean curves of all specimens containing one prolate void, compared to dense specimens, at nominal strain rate of $2.8 \times 10^{-3}\ s^{-1}$.

nominal dimensions. The row of the 3 voids (Fig. 4a) is not completely aligned with the edges of the gauge section due to some inaccuracy of post-manufacturing machining of specimen slots.

2.2.4. SCS with prolate spheroidal voids

A series of specimens containing prolate spheroidal voids were additively manufactured. The location of the prolate void was set at the geometric center of the specimen gauge, similar to that of the single spherical void (described in the previous section). The ratio between the *long* diameter (C), and the *short* diameter (A) of the prolate void was set to be $C/A = 3$, and $A = 450$ μm and its longitudinal axis was aligned with the gauge mid-section. The volume of the prolate void was set to be equal to the volume of the single spherical void (Ø650 μm) or equal to the total volume of the three spherical voids (3 × Ø450 μm). In each specimen type, the angle of the elongated void was systematically rotated with respect to the mid-section of the specimen gauge, by 0°, 45°, 90° and 135°, as illustrated in Fig. 5 and summarized in Table 3. Fig. 6 shows CT images and measurements of the single prolate void oriented by 0°. All measurements of prolate void diameters were kept within tolerance of approximately ± 100 μm, compared to the model's nominal dimensions.

2.2.5. Void volume fraction

As mentioned, the void volume of all specimen types was set to be equal. The void volume fraction is calculated according to the volume of the artificial void (or voids) with respect to the volume of the gauge section, which is equal to 0.0015 (0.15%). Further information about the void volume fraction calculations can be found in (Fadida et al., 2019).

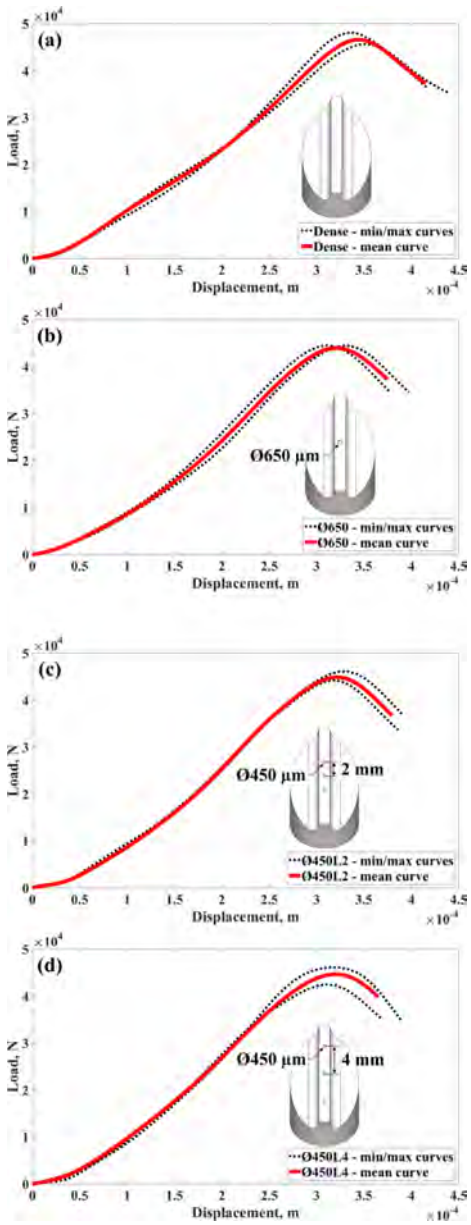

Fig. 11. Load-displacement curves of all specimens containing one spherical void or three voids (b-d), compared to dense specimens (a), at nominal strain rate of $1.8 \times 10^4\ s^{-1}$.

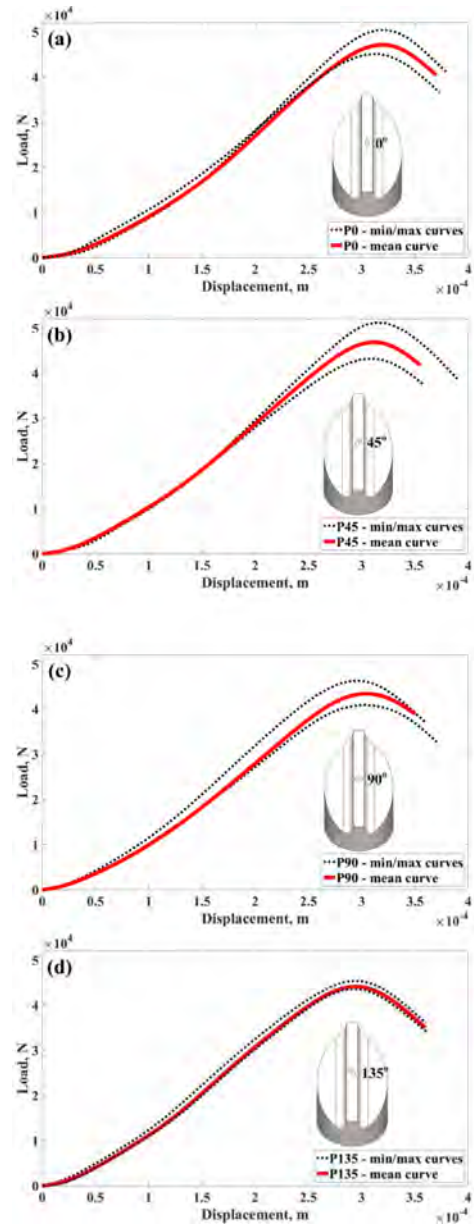

Fig. 12. Load-displacement curves of all specimens containing one prolate void at nominal strain rate of $1.8 \times 10^4\ s^{-1}$.

3. Results

The presence of discrete voids induces stress concentration in their surroundings (Bourcier et al., 1986) so the report of homogeneous stress-strain values in the case of artificial voids is inaccurate. Therefore, the following results refer only to macroscopic load-displacement response of the specimens. Note that the same approach was used in our previous reports.

3.1. Quasi-static compression of SCS with spherical and prolate voids

All specimen types, labelled as Dense, Ø650, Ø450L2, Ø450L4, P0, P45, P90 and P135 were tested in compression on a servo-hydraulic MTS machine. The results of each specimen type are based on set of 4 specimens. The nominal strain rate was evaluated according to the numerical results and it is equal to $2.8 \times 10^{-3}\ s^{-1}$ (see appendix). Optical laser extensometer was used to measure the vertical displacements, while load values were recorded by machine's load cell. Figs. 7 and 8 show the load-displacement results of the specimens containing spherical and prolate voids respectively. The mean curve of 4 specimens is shown in thick red line and the dispersion of the experimental results is illustrated by minimum and maximum curves shown in dotted black lines. The elastic response of the specimens can vary between different specimen types because it depends on the dimensional accuracy and does not truly reflect the elastic modulus of the material. Therefore, a comparison between different specimen types is shown for the plastic response only. Figs. 9 and 10 summarize the load-plastic displacement results of all mean curves of all specimen types presented in Figs. 7 and 8 respectively. For all the void-containing specimens, a reduction in

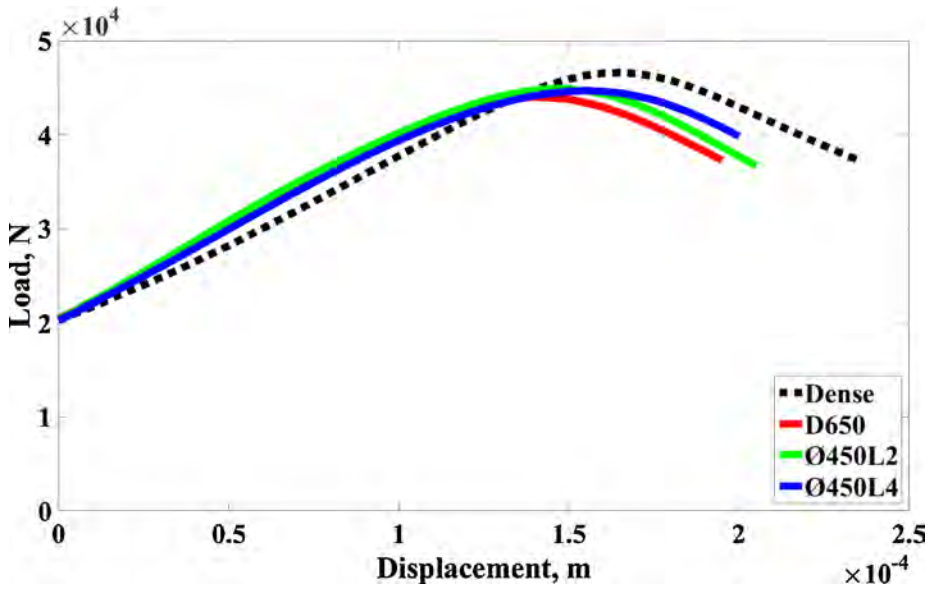

Fig. 13. Load-plastic displacement mean curves of all specimens containing one spherical void or three voids, compared to dense specimens, at nominal strain rate of $1.8 \times 10^4\ s^{-1}$.

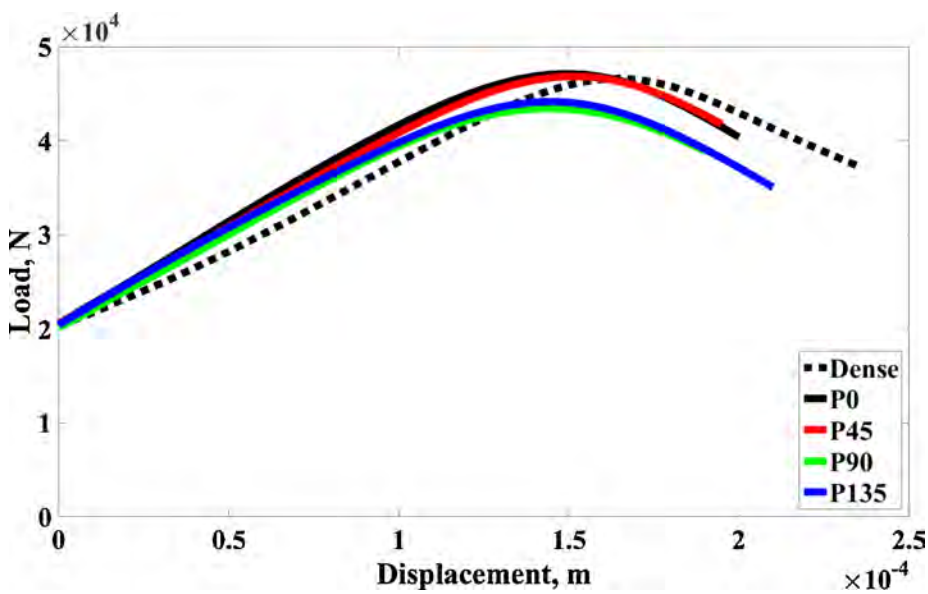

Fig. 14. Load-plastic displacement mean curves of all specimens containing one prolate void, compared to dense specimens, at nominal strain rate of $1.8 \times 10^4\ s^{-1}$.

displacement to failure can be observed with respect to the dense specimens, while changes in load are quite minor. Both specimens containing 3 spherical voids, i.e., Ø450L2 and Ø450L4, show a similar displacement to failure, which is smaller than that of the specimen containing a single spherical void i.e. Ø650. However, changing the distance between the spherical pores (i.e., 2 or 4 mm) did not result in a significant change of the load-displacement curves. In general, the displacement to failure of the specimens containing a prolate void is smaller than that of the specimens containing a spherical void or voids. However, the void's orientation in the gauge section has negligible effect on the measured load-displacement curve. To summarize the quasi-static tests, it was observed that:

a) The **presence of the void** (or voids) causes a noticeable reduction in the displacement to failure and slight reduction in load, with respect to a fully dense specimen.
b) The **number of spherical voids** (one or three) and the **shape of the void** (spherical or prolate) affect markedly the displacement to failure.
c) The **distance between spherical voids** (2 or 4 mm) and the **prolate void orientation** (0°, 45°, 90° and 135°) have a minor influence on the mechanical response.

3.2. Dynamic compression of SCS with spherical and prolate voids

All specimen types and voids arrangements for the dynamic tests are identical to that used for the quasi-static tests. Each specimen type included a set of 4 specimens that were tested using the split Hopkinson pressure bar (SHPB). The nominal strain rate was evaluated according to the numerical results and it is equal to $1.8 \times 10^4\ s^{-1}$ (see appendix). Figs. 11 and 12 show the load-displacement results of the specimens containing spherical and prolate voids respectively. Figs. 13 and 14

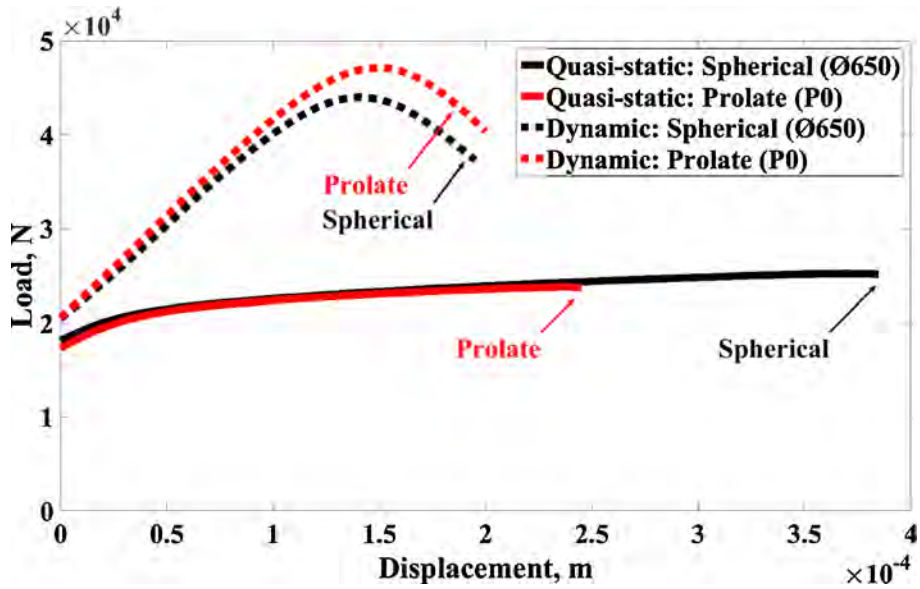

Fig. 15. A comparison between the load-plastic displacement mean curve of specimens containing single spherical or prolate void, which both have the same void volume fraction, at different strain rates.

summarize the load-plastic displacement results of all mean curves of all specimen types that presented in Figs. 11 and 12 respectively. Unlike the quasi-static response that was characterized by a noticeable plastic flow (subsequent to the elastic region), the dynamic mechanical response was characterized by a dominant initial peak and quite limited plastic flow without any observed Pochhammer-Chree oscillations. The initial peak (or the time it takes to achieve equilibrium of forces on the specimen) reflects the longitudinal and radial inertia, which are due to the rapid accelerations in the test apparatus. The displacement to failure of all void-containing specimens is smaller than that of the dense specimens while the differences in load are again quite minor. Unlike the quasi-static results, the plastic mechanical response seems quite limited and cannot be clearly defined due to the inertial peak. The effect of the number of spherical voids (one or three) and the distance between them (2 or 4 mm) seems quite minor. Similar to the quasi-static results, the orientation of the prolate void has no apparent effect on the measured load-displacement curve. Fig. 15 shows a comparison between the results of specimens containing single spherical (Ø650) or prolate (P0) void at different strain rates. In the dynamic tests, the shape of the void (spherical or prolate) has no significant effect on the mechanical response, unlike in the quasi-static case.

To summarize the dynamic tests, it was observed that:

a) The **presence of the void** (or voids) reduces the displacement to failure and causes a slight reduction in the load, with respect to a fully dense specimen.
b) The specified void parameters i.e., **number, distance, orientation and shape**, seem to have a minor impact on the mechanical response.

4. Fractographic analysis

Fractographic analyzes were performed on representative specimens of each loading mode using scanning electron microscopy (HR-SEM, MIRA TESCAN). The fractographs of the shear-compression specimens (SCS) were compared to those of the recently tested shear-tension specimen (STS) (Fadida et al., 2019). Figs. 16-19 refer to the quasi-static tests results, while Figs. 20-21 refer to the dynamic ones. Fig. 16 shows the fracture surface of fully-dense SCS and STS subjected to quasi-static loading. For the SCS (Fig. 16a-b), a "veined" patterns was observed (Tabachnikova et al., 2001), which is characterized by regions (linked to each other) of elongated dimples oriented along the inclination of the gauge. The observation of elongated dimples confirms the occurrence of a ductile fracture mechanism, in which failure is governed by a *dominant shear component*. However, for the STS (Fig. 16c-e), relatively small equiaxed dimples are observed, indicating that the dominant fracture mechanism is related to void coalescence by internal necking, which is typical of *tensile fracture*. Fig. 17a-b shows the final evolution of the single spherical void Ø650 within SCS and STS respectively. For the SCS (Fig. 17a), the initially spherical void is compressed along the shear direction, which is expected to result from the shear-dominant stress state (Besson, 2010; Chen and Osovski, 2019). But, for the STS (Fig. 17b) the void remains quite spherical during plastic deformation and fracture, indicating once again that shear is apparently not the dominant failure mode for shear-tension specimens. For the SCS (Fig. 17a), the deformed void's trace seems to be divided into three regions that were observed for all initial spherical void configurations subjected to shear-compression stress state (Figs. 17a and 18a). The first region is characterized by elongated dimples (noted R1 in Fig. 17a), the second region is characterized by smeared material (R2) and the last by an open cavity filled with powder residue (R3). According to the powder left inside the void (Fig. 17a), it seems that fracture occurred before the void was completely closed. Similar observation can be made on Fig. 18a for the configuration of 3x Ø450 μm voids located 2 mm from each other. The right part of the image describes all three voids along the gauge section, while the left part describes one of the side voids. The dimpled region that was observed for the spherical void is not found for the prolate void showed in Fig. 19a. Instead, the prolate void in the SCS is divided into 2 main regions, smeared (noted R1 in Fig. 19a), and powdery (R2). The shape of the prolate void in the SCS seems to preserve its original shape similar to that of the STS. However no smeared or powdery regions were observed within the void in the STS (Fig. 19b). As mentioned, Figs. 20-21 show the fracture surface of SCS and STS subjected to high strain-rate loading. For the dense SCS (Fig. 20a), elongated dimples were observed, which seem more stretched compared to the quasi-static ones (Fig. 16b.) But, for the STS (Fig. 20b), the dimples look similar in shape and size to the quasi-static ones (Fig. 16d-e). For the SCS containing one

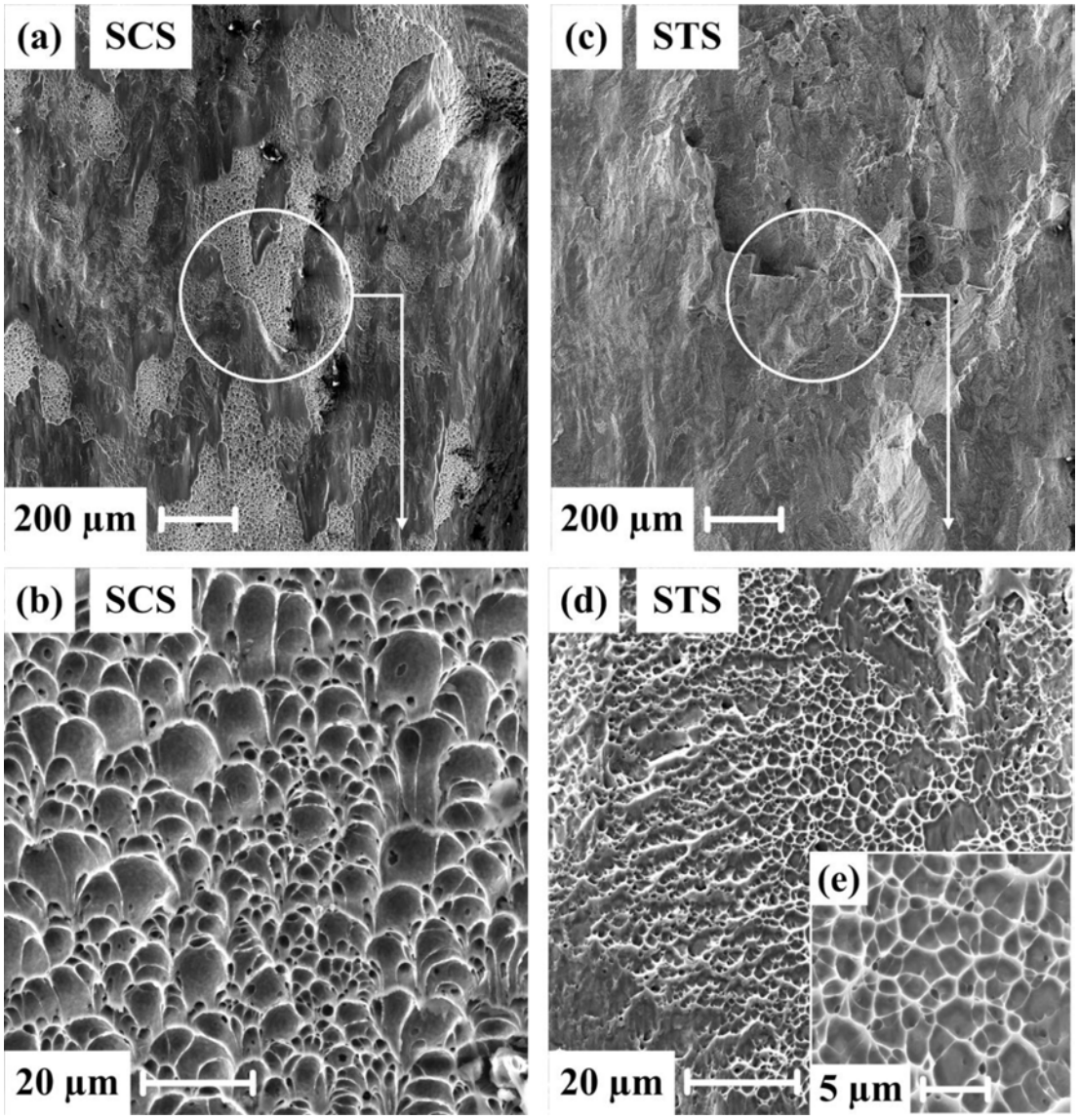

Fig. 16. SEM images of fully-dense Ti6Al4V specimens in the mid-section of the gauge after quasi-static loading. SCS (a-b). STS (c-e).

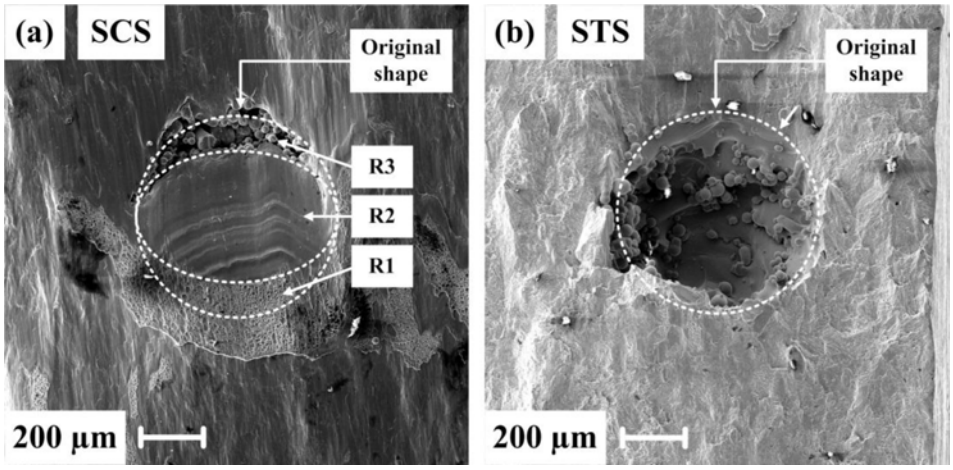

Fig. 17. SEM images of specimens containing one spherical void (Ø650) after quasi-static loading. SCS (a). STS (b).

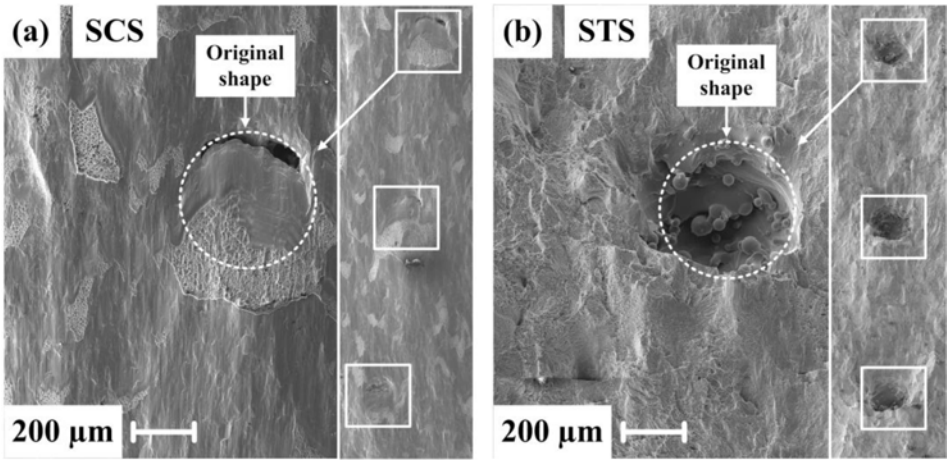

Fig. 18. SEM images of specimens containing 3 spherical voids (Ø450L2) after quasi-static loading. SCS (a). STS (b).

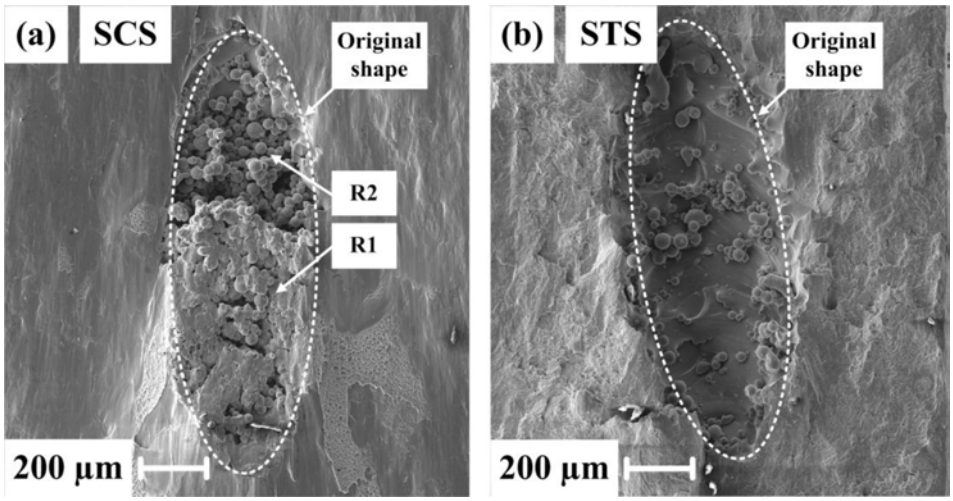

Fig. 19. SEM images of specimens containing one prolate void (P0) after quasi-static loading. SCS (a). STS (b).

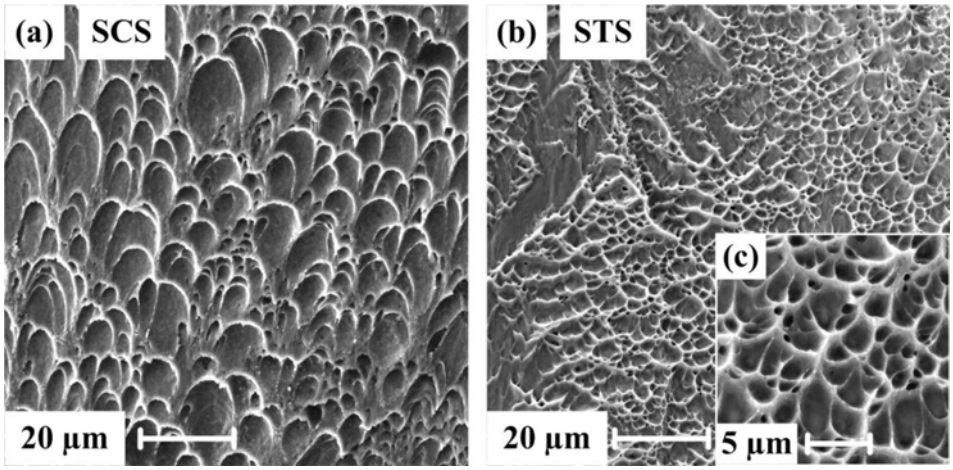

Fig. 20. SEM images of fully-dense Ti6Al4V specimens in the mid-section of the gauge after dynamic loading. SCS (a). STS (b-c).

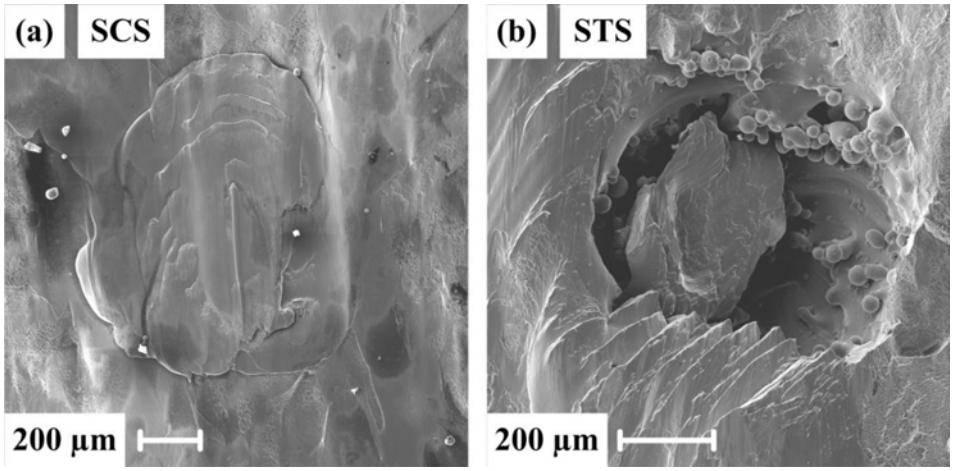

Fig. 21. SEM images of specimens containing one spherical void at the geometrical center of the gauge after dynamic loading. SCS (a). STS (b).

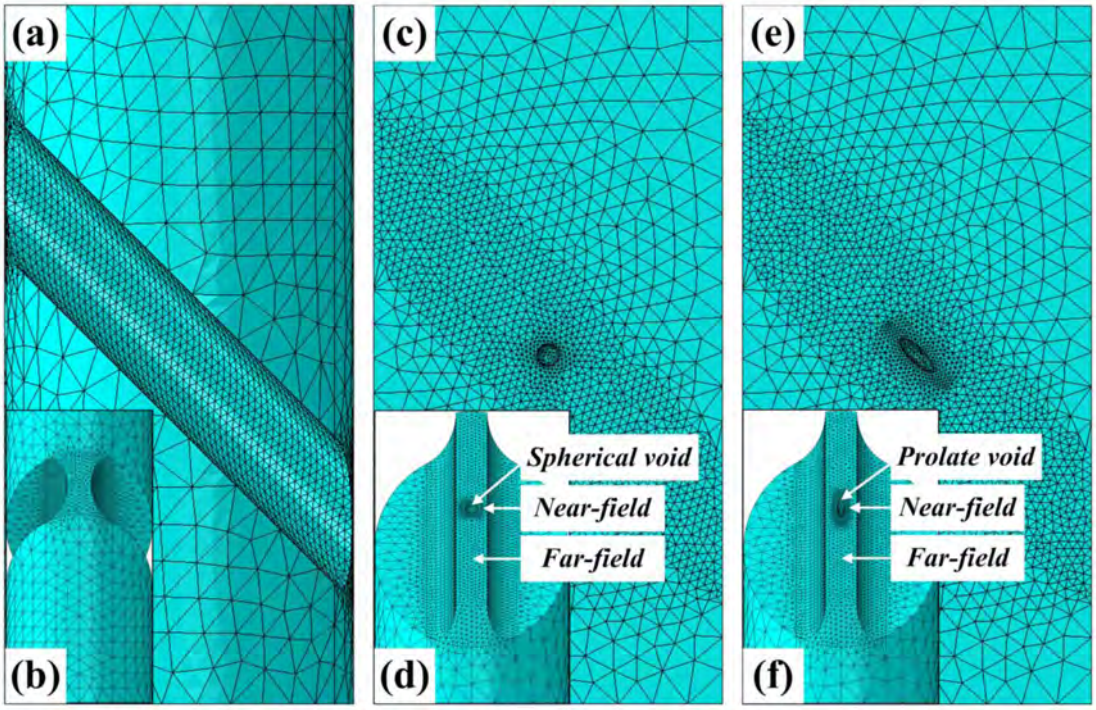

Fig. 22. The mesh of the numerical models at front view (a) and side view (b). Cross-section views (front and mid-gauge) for spherical void (c-d) and prolate void (e-f).

Table. 4
Constitutive model parameters used to describe the plastic behavior of the SCS and STS.

	σ_0 *[MPa]*	*K*	*n*	ε_{eq}^{p}
SCS	1120	395	0.345	0.27
STS	920	395	0.345	0.18

spherical void (Fig. 21a), the void is completely smeared, which makes it difficult to evaluate the level of deformation (or the final deformed void's geometry). For the STS (Fig. 21b), the void preserves its spherical shape and a zig-zag crack is observed at the void's edge, which is also typical for tensile fracture (Tvergaard and Needleman, 1984). To summarize the fractographic results, it was found that:

a) The SCS fails by shear-dominated fracture, while the STS fails by tension-dominated fracture.
b) Artificial voids embedded in the SCS show a marked shape deformation, which is not observed for those within the STS, which reinforces the previous point.
c) For the SCS, the absence of smeared region in the prolate void fracture seems to indicate early stage failure, compared with that of the spherical void.

5. Numerical simulations

5.1. The model

The quasi-static behavior of the void-containing specimens was studied numerically using a commercial finite element software Abaqus/standard (ABAQUS 6.14, 2014). The simulations considered quasi-static loading to avoid complications related to stress-wave loading while retaining the salient features of the stress fields in the

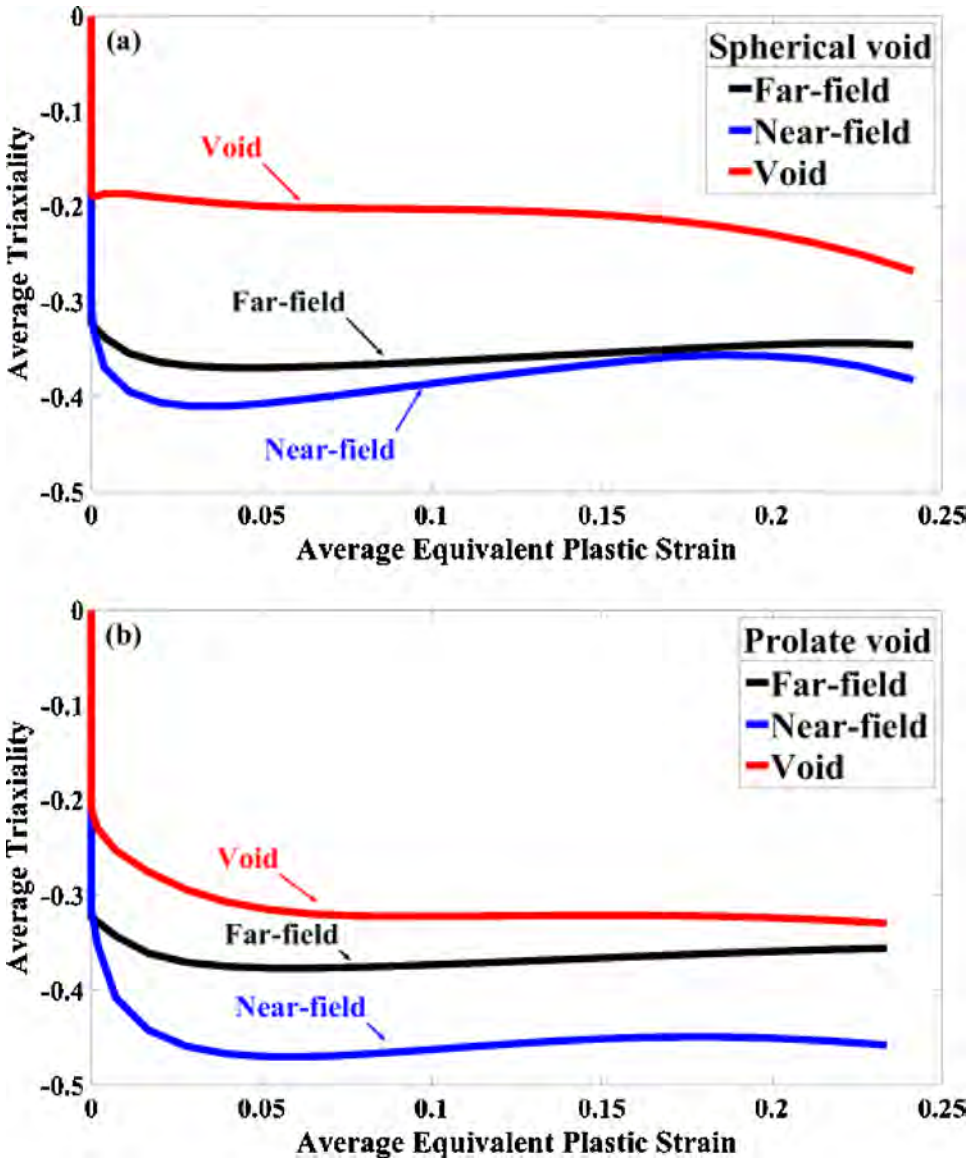

Fig. 23. The average triaxiality as a function of the average equivalent plastic strain for spherical (a) and prolate (b) void within SCS. Note that the plastic strain was calculated at the far-field.

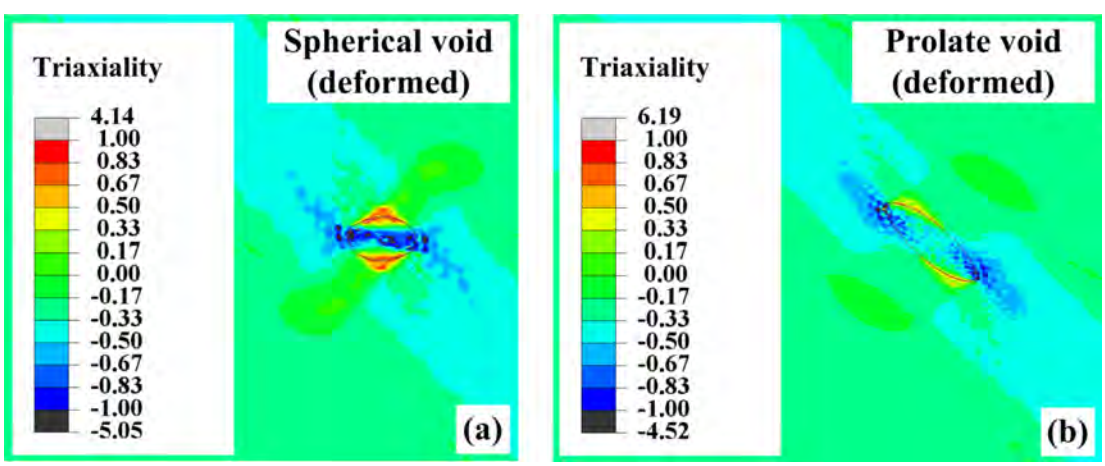

Fig. 24. The triaxiality for the deformed spherical (a) and prolate (b) void within SCS (cross-section side view).

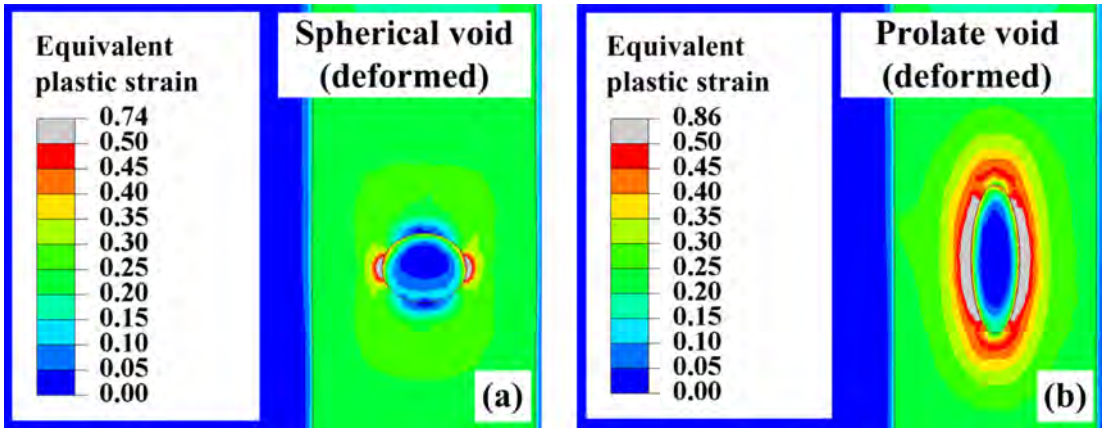

Fig. 25. The equivalent plastic strain for the deformed spherical (a) and prolate (b) void within SCS (mid-section of the gauge).

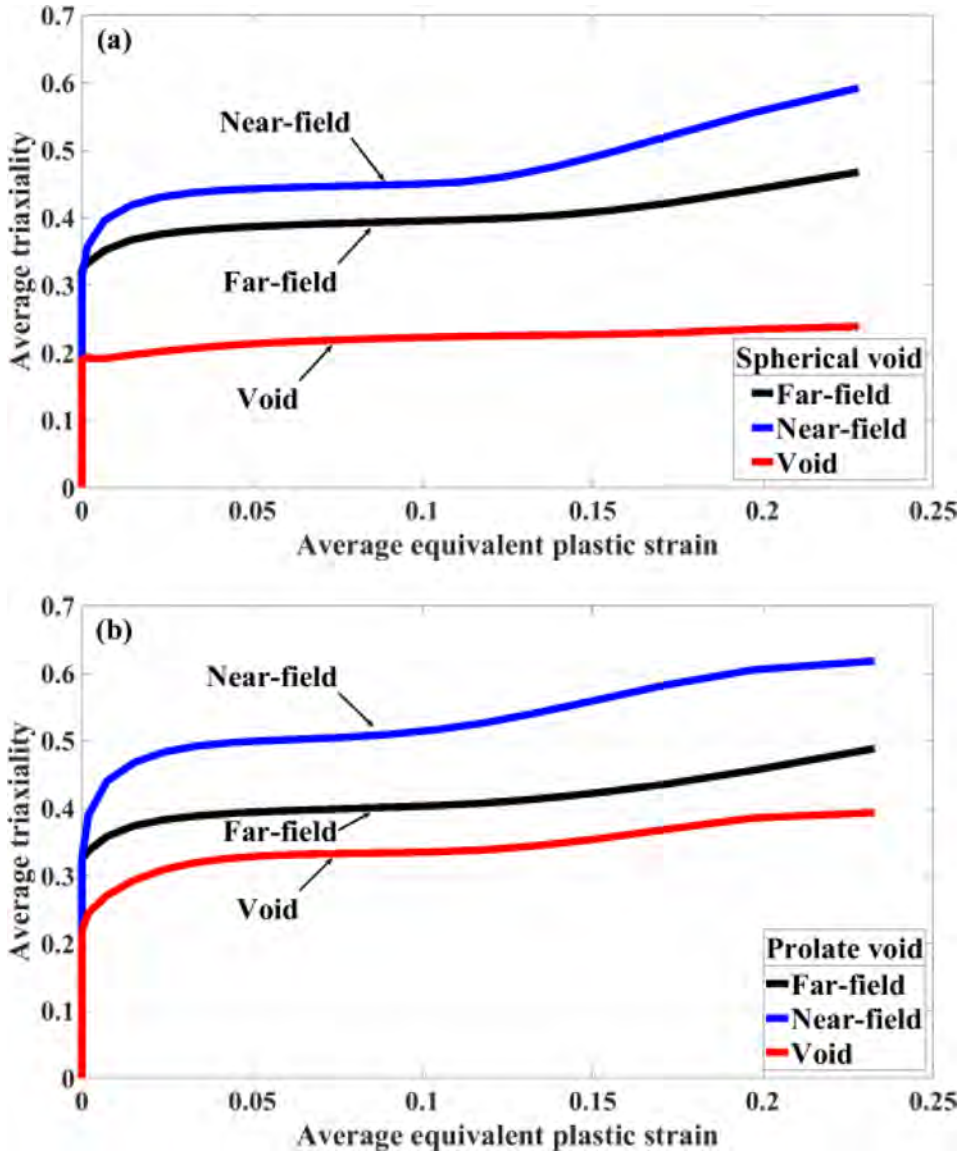

Fig. 26. The average triaxiality as a function of the average equivalent plastic strain for spherical (a) and prolate (b) void within STS. Note that the plastic strain was calculated at the far-field.

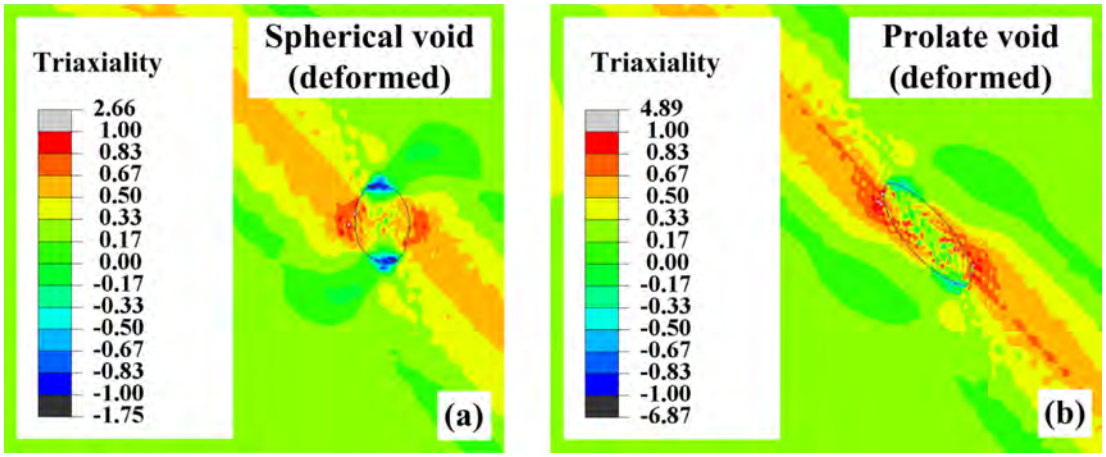

Fig. 27. The triaxiality for the deformed spherical (a) and prolate (b) void within STS (cross-section side view).

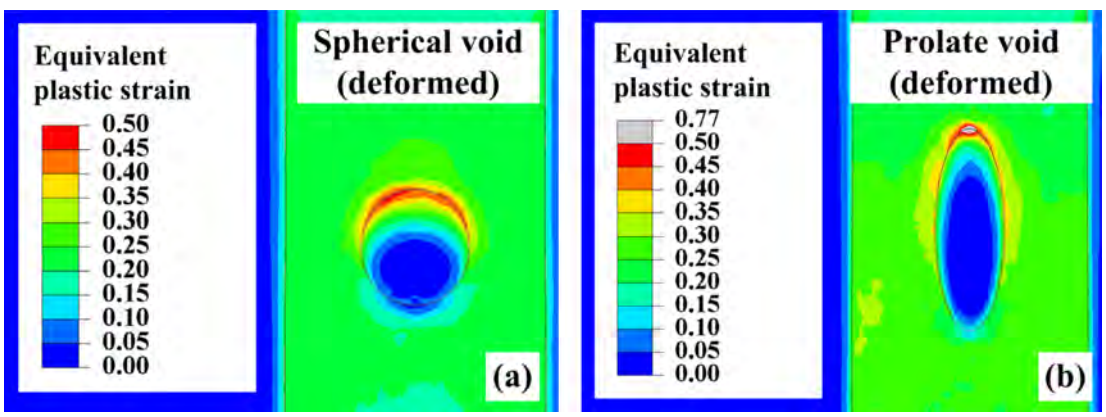

Fig. 28. The equivalent plastic strain for the deformed spherical (a) and prolate (b) void within STS (mid-section of the gauge).

Table. 5
A summary of SCS results for both strain rates. The level of impact on the mechanical response is indicated by "+" for major impact and "-" for minor impact.

	Quasi-static		Dynamic	
Parameters	Load	Disp.	Load	Disp.
Presence of artificial voids	-	+	-	+
Void shape	-	+	-	-
Number of voids	-	+	-	-
Distance between voids	-	-	-	-
Void orientation	-	-	-	-

gauge section and near vicinity of the voids. The model was meshed with 10-node quadratic tetrahedral elements (C3D10) with a typical size of 250 μm in the specimen's gauge and 1000 μm on the rest of the specimen. Mesh refinement was applied at the void boundary and its surroundings with elements in the size of 100 μm. During the plastic deformation of the gauge, the void, whether spherical or prolate, has a definite influence on its surrounding. To examine this influence, triaxiality and equivalent plastic strain were characterized in the immediate surroundings of the void. The nearest region to the void at the mid-section of the gauge was defined as twice the diameter of the void and defined as the *near-field*. The region outside the *near-field* was defined as the *far-field*. Fig. 22 shows the meshed numerical model and the specified regions around the spherical or prolate void. A displacement of 1 mm was applied vertically on the upper face of the specimen and the bottom face was set with fixed boundary conditions. The AM Ti6Al4V material behavior was described by the J2 plasticity with isotropic hardening, while damage and rupture were determined using the software implementation for ductile damage model. The elastic behavior of the material was also considered in the simulations. The Young's modulus was taken as 117 GPa with Poisson's ratio 0.34. The true-stress strain behavior of the material in the plastic region was described by a power-law hardening material model of the form $\sigma = \sigma_0 + K(\varepsilon_p)^n$ where,σ_0 is the tensile yield stress, K is a constant and n is the strain-hardening coefficient. The initial input data for the material model was based on the results of quasi-static tensile tests (Fadida et al., 2018). Using a simple trial and error method, the material model was modified until the load-displacement curve obtained from simulations was consistent with the experimental results. Strength asymmetry (i.e., tension vs. compression) of Ti6Al4V is known in the literature, and as for most hcp metals, is due to somewhat different dislocation mechanism at each one of the loading modes (Jones and Hutchinson, 1981). To overcome this issue simply, an *ad-hoc* increase of strength of approximately 10% (100 MPa) was added to the tensile yield stress to describe the plastic behavior of the material in shear-compression, while K and n remain unchanged. To allow for comparison, the behavior of voids within shear-tension specimens is also presented (see Section 5.3). The material model (of STS) was modified according to the same previously described method. It was assumed that the damage model is not strain-rate or triaxiality dependent and consists of a critical value of the equivalent fracture strain (ε_{eq}^{p}) at

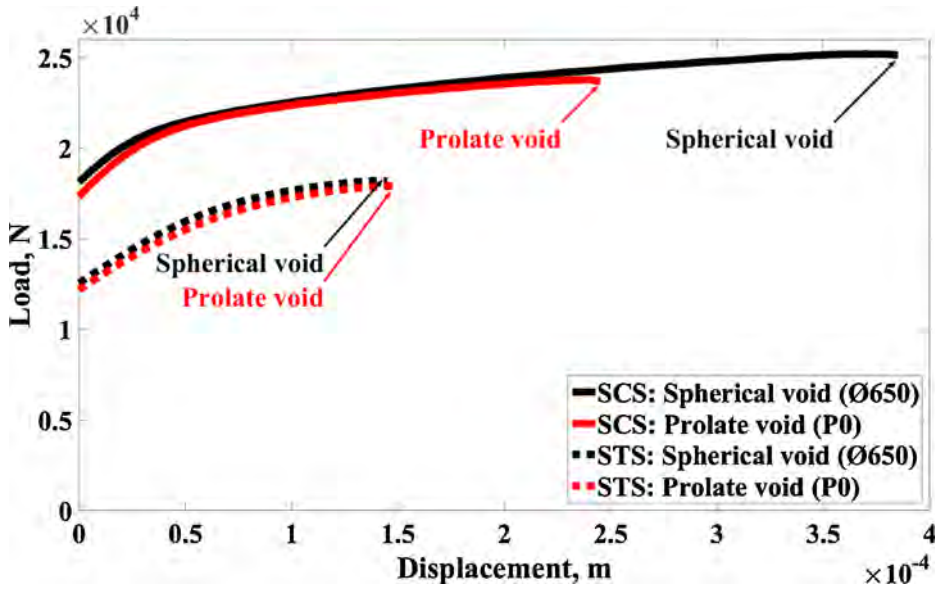

Fig. 29. A comparison between SCS and STS containing spherical or prolate void in quasi-static loading.

Table. 6
A. comparison between SCS and STS for the specified experimental parameters. The level of impact on the displacement to failure is indicated by "+" for major impact and "-" for minor impact.

	SCS		STS	
Parameters	Static	Dynamic	Static	Dynamic
Presence of artificial voids	+	+	+	+
Void shape	+	-	-	-
Number of voids	+	-	-	-
Distance between voids	-	-	-	-
Void orientation	-	-	-	-

damage initiation. The material model parameters are summarized in Table 4.

5.2. Results of SCS

The stress triaxiality (η) and the equivalent plastic strain (ε_{eq}^{p}) are defined as follows:

$$\eta = \frac{\sigma_m}{\sigma_{eq}} \tag{5.2.1}$$

$$\varepsilon_{eq}^{p} = \sqrt{\frac{2}{3}\varepsilon_{ij}'\varepsilon_{ij}'} \tag{5.2.2}$$

where σ_m is the mean stress (or hydrostatic stress), σ_{eq} is the equivalent von Mises stress and ε_{ij}' represent the deviatoric strain tensor components. For the specified regions at the mid-section of the gauge, Fig. 23 shows the average stress triaxiality as a function of the *far-field* average equivalent plastic strain. The average triaxiality of the void was calculated on the void's 3D-surface, while the average triaxiality of the *near and far-fields* was calculated in regions at the gauge's middle surface (as shown in Fig. 22). During plastic deformation, the *far-field* triaxiality of the two voids' geometries (i.e., spherical or prolate) seems quite constant and is equal to approximately -1/3 (Dorogoy et al., 2015). For the spherical void case, the *near-field* triaxiality seems similar to that of the *far-field*. However, for the prolate void case, the *near-field* triaxiality is much lower than that of the *far-field*. In addition, the average triaxiality of the spherical void is significantly higher compared to that of the prolate void. It can be assumed that locally the stress state can change according to geometry of the void. These results illustrate the void's impact on its surrounding, which seems greater for the prolate void. A comparison between spherical and prolate void is presented in Figs. 24-25. Fig. 24 shows the triaxiality at cross-section side view and Fig. 25 shows the equivalent plastic strain at the mid-section of the gauge. Both figures as shown for the same displacement (~0.3 mm), which represents approximately the onset of failure of the specimen containing prolate void. It can be seen that the spherical void deforms quite significantly (turning later into an S-shape), while the prolate void preserves its original shape. In accordance to that, higher triaxiality values were observed around the spherical void compared to the prolate void. However, for the prolate void, high plastic strain values were noticed all around the prolate void, compared to only discrete locations around the spherical void. Recall fractographic results of spherical void within the SCS (Fig. 17a), the void's deformation is well captured in the numerical simulation (Fig. 25a) i.e., compressed in the shear direction with a shape similar to the smeared material region.

5.3. Results of STS

For spherical and prolate voids within the STS, Fig. 26 shows the average stress triaxiality as a function of the *far-field* average equivalent plastic strain. The *far-field* triaxiality seems quite constant and is equal to approximately 1/3 (Dorogoy et al., 2016). Unlike the SCS case, the impact of the void on its surroundings seems quite similar for the two voids' geometries. Figs. 27-28 were captured at the same displacement (~0.25 mm), which represents approximately the onset of failure of specimens containing prolate void. For the STS, the comparison between spherical void and prolate void in terms of triaxiality and plastic strains shows that the differences are less pronounced compared to those observed in the SCS. These findings are consistent with the recently reported results (Fadida et al., 2019) indicates that in the case of STS, the pore geometry (spherical or prolate) has a negligible effect on the mechanical response. To summarize, the numerical simulations, it is observed that:

a) The differences between spherical and prolate void in terms of triaxiality and equivalent plastic strain are more distinct in the SCS

than in the STS.

b) For the SCS, the stress state causes the prolate void to undergo relatively high plastic strain in its surrounding, which promotes early failure, compared with the spherical void.

6. Discussion

This study concerns embedded voids under various stress states and loading regimes. As such, it is not meant to address or validate the various earlier-mentioned models describing the mechanics of porous materials or the void interaction and subsequent damage mechanisms. Rather, this study is aimed at shedding light on the influence of embedded non-interacting voids of different shapes and orientation, all with an identical volume fraction, on the mechanical response of sheared specimens, keeping in mind the importance of shear in ductile fracture.

6.1. The mechanical response of void-containing SCS

In both rates of loading, the presence of an artificial void (or voids) in shear-dominated stress states has a considerable impact on the SCS mechanical response. The typical load-displacement curve of void-containing specimens compared to that of the dense is characterized by significant reduction in displacement to failure and slight reduction in load. According to the quasi-static results, the displacement to failure of the specimen types containing 3 × Ø450 voids μm void is smaller compared to that of the specimen containing single Ø650 void. This behavior was not observed in the dynamic results, i.e., all void-containing specimens had similar displacement to failure. In both strain rate regimes, changing the distance between the spherical voids (i.e., 2 mm or 4 mm) did not result in a significant change in the load-displacement curves. It can be noted that Nielsen et al. (Nielsen et al., 2012) found in their numerical study that the overall material response for various (spherical) void spacings is quite similar until the onset of coalescence. For the specified spheroid void and gauge dimensions, the orientation of the void has no noticeable effect on the mechanical response of the specimens in both strain rate regimes. In the quasi-static regime, the displacement to failure of the 0° oriented prolate void is significantly smaller compared to that of the spherical Ø650 void, which indicates shape sensitivity in the shear-dominated stress state. As shown in the numerical results, due to its geometry, the prolate void induces high plastic strain at its environment during shear deformation, which eventually leads to an early failure, compared to the spherical void. In this context, Tvergaard (Tvergaard, 2009) who studied the behavior of voids in a shear field, pointed that in the case of 3D-array of voids, a localization of high shear strains is expected to be developed in the ligaments between the void in the direction transverse to the shear direction, compared to the 2D case. The dynamic results show that for both void geometries the mechanical response is quite similar. It can be concluded that the dynamic response is insensitive to the investigated void configuration (shape, number, distance and orientation) and the specific fixed void volume fraction (0.15%). A similar phenomenon was observed by Rotbaum et al. (Rotbaum et al., 2015) for cylindrical specimens with notches, and by Fadida et al. (Fadida et al., 2018) for cylindrical specimens with embedded spherical voids, which indicates that in dynamic loading configurations, the sensitivity to the weak(est) link is apparently reduced. The following Table 5 summarizes the key results of the SCS. It should mention that even though the predetermined void volume fraction (i.e., 0.15%) was kept constant in all types of the void-containing specimen, the results are not sufficient to be generalized in a straightforward manner to any other configurations of voids or loading conditions.

6.2. Effect of void shape between SCS and STS

The experimental results supported by the SEM and the numerical analyses shows that the SCS design allows stress state with dominant shear component within the specimen gauge. However, the effect of shear in the STS seems to be less dominant. The deformation of spherical and prolate void is well observed in the SCS fractography, while the void shape in the STS seems almost unchanged. Fig. 29 shows the load-plastic displacement curves of SCS compared to STS, which contains spherical or prolate void. It is quite clear that the SCS allows larger displacements than those of the STS, affecting the development of the void and ultimately the nature of failure. Table 6 summarizes the key results of SCS compared to STS for both strain rates. To summarize, the observed trends in displacement to failure of SCS vs. STS regarding the effect of void shape are reflected in both fractographic and numerical results.

7. Conclusions

This study has examined the mechanical response of specimens containing discrete artificial voids under shear-dominated stress states at different strain rates. A comparison between the current results of SCS and the previously reported results of STS lead to the following conclusions, for the investigated void configurations and the fixed void volume fraction of 0.15%.

For SCS under quasi-static loading:

- The shape of the void significantly affects the displacement to failure.
- The number of voids at constant volume fraction reduces noticeably the displacement to failure.

For SCS and STS under quasi-static and dynamic loading:

- The presence of the voids is reflected by a reduction in the displacement to failure, compared to the dense specimens.
- The distance between spherical voids does not seem to affect significantly the mechanical response of the specimens.
- The orientation of the prolate void does not seem to have any noticeable impact on the mechanical response of the specimens.

8. Author agreement

We declare that,

a) This manuscript is original and has not been published before.
b) This manuscript is not currently being considered for publication elsewhere.
c) This manuscript has previously been submitted for possible publication in JMPS but unfortunately was rejected. To our opinion, the reviewers did not understand the novelty of the research and rejected it with arguments that seems irrelevant to the intentions of this study.

Appendix

The strain rate within the SCS gauge was obtained from the numerical results by derivation of the equivalent plastic strain with respect to time. Fig. A.1 shows the nominal strain rate that was calculated by linear regression for the quasi-static and dynamic loading and found to be $2.8 \times 10^{-3}\ s^{-1}$ and $1.8 \times 10^{4}\ s^{-1}$ respectively.

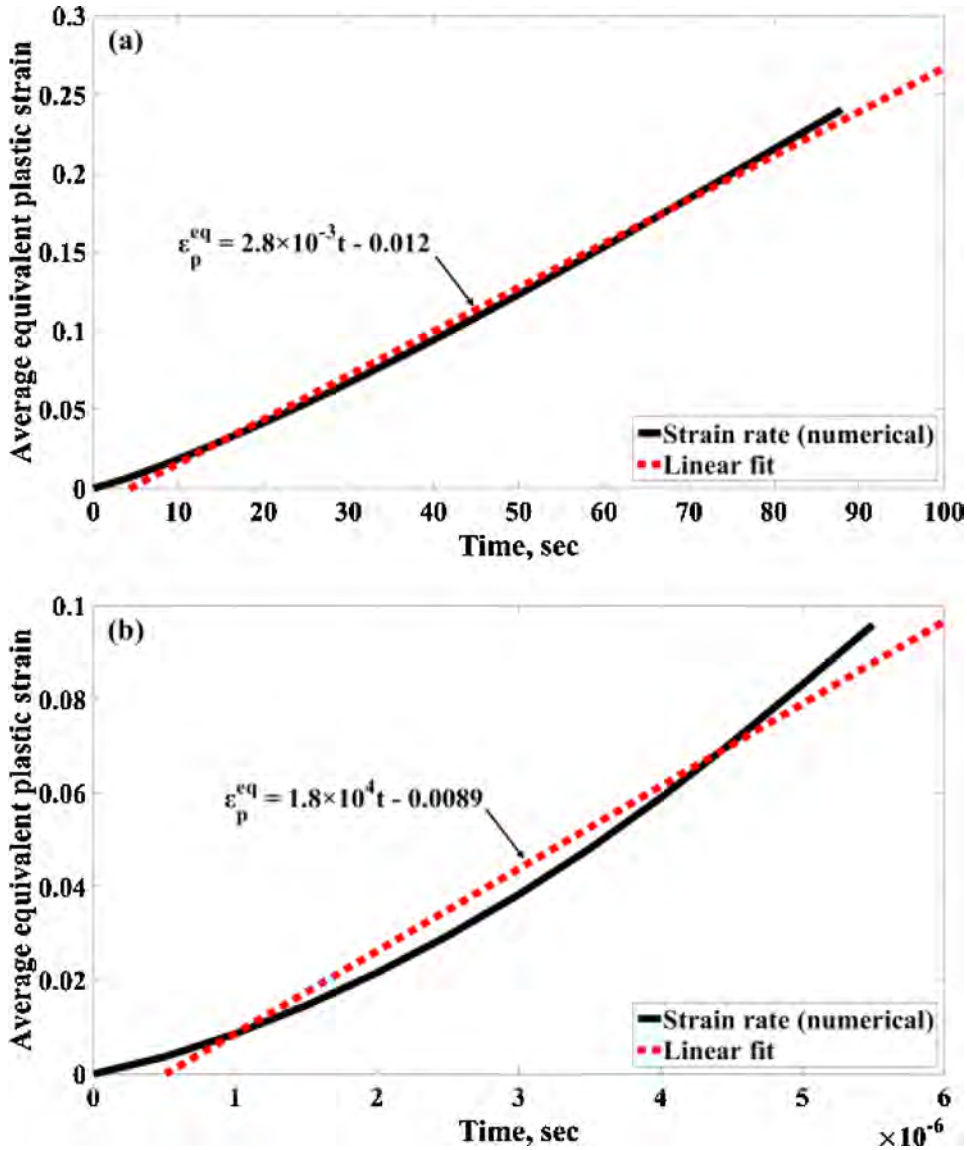

Fig. A.1. The strain rate at the mid-section of the gauge obtained from the numerical simulations for quasi-static (a) and dynamic (b) loading.

Declaration of Competing Interest

The authors declare that there are no conflicts of interest.

Acknowledgment

The authors wish to thank Dr. A. Dorogoy for his valuable technical support and also Dr. Juan Carlos Nieto Fuentes for his assistance in producing the SEM images, as well as Dr. Sagi Chen for the useful discussions.

Supplementary materials

Supplementary material associated with this article can be found, in the online version, at doi:10.1016/j.mechmat.2020.103413.

References

ABAQUS 6.14, 2014. ABAQUS/CAE 6. 2014. Dassault Systèmes Simulia Corp 14-2 Providence, RI, USA.

Besson, J., 2010. Continuum models of ductile fracture: a review. Int. J. Damage Mech. 19. https://doi.org/10.1177/1056789509103482.

Bourcier, R.J., Koss, D.A., Smelser, R.E., Richmond, O., 1986. The influence of porosity on the deformation and fracture of alloys. Acta Metall. 34. https://doi.org/10.1016/0001-6160(86)90147-1.

Brown, L.M., Embury, J.D., 1973. Initiation and growth of voids at second phase particles. Inst. Met. (London). Monogr. Rep. Ser. 1, 164–169.

Butcher, C., Abedini, A., 2017. Shear confusion: Identification of the appropriate equivalent strain in simple shear using the logarithmic strain measure. Int. J. Mech. Sci. 134, 273–283. https://doi.org/10.1016/j.ijmecsci.2017.10.005.

Chen, S., Osovski, S., 2019. The effect of internal pressure in gas pores containing materials on their mechanical stability under shear. Mech. Res. Commun. 98, 37–41. https://doi.org/10.1016/j.mechrescom.2019.05.008.

Chu, C.C., Needleman, A., 1980. Void nucleation effects in biaxially stretched sheets. Trans. ASME. J. Eng. Mater. Technol. 102. https://doi.org/10.1115/1.3224807.

Dorogoy, A., Rittel, D., 2005. Numerical validation of the shear compression specimen. Part I: Quasi-static large strain testing. Exp. Mech. 45, 167–177. https://doi.org/10.1177/0014485105052325.

Dorogoy, A., Rittel, D., Godinger, A., 2016. A shear-tension specimen for large strain testing. Exp. Mech. 56. https://doi.org/10.1007/s11340-015-0106-1.

Dorogoy, A., Rittel, D., Godinger, A., 2015. Modification of the shear-compression specimen for large strain testing. Exp. Mech. 55. https://doi.org/10.1007/s11340-015-0057-6.

Dunand, M., Mohr, D., 2014. Effect of lode parameter on plastic flow localization after proportional loading at low stress triaxialities. J. Mech. Phys. Solids 66. https://doi.org/10.1016/j.jmps.2014.01.008.

Facchini, L., Magalini, E., Robotti, P., Molinari, A., Hoges, S., Wissenbach, K., 2010. Ductility of a Ti-6Al-4V alloy produced by selective laser melting of prealloyed powders. Rapid Prototyp. J. 16, 450–459. https://doi.org/10.1108/13552541011083371.

Fadida, R., Rittel, D., Shirizly, A., 2015. Dynamic mechanical behavior of additively manufactured Ti6Al4V with controlled voids. J. Appl. Mech. 82, 041004. https://doi.org/10.1115/1.4029745.

Fadida, R., Shirizly, A., Rittel, D., 2019. The static and dynamic shear-tension mechanical response of AM Ti6Al4V containing spherical and prolate voids. Int. J. Eng. Sci. 141, 1–15.

Fadida, R., Shirizly, A., Rittel, D., 2018. Dynamic tensile response of additively manufactured Ti6Al4V with embedded spherical pores. J. Appl. Mech. Trans. ASME 85. https://doi.org/10.1115/1.4039048.

Gologanu, M., Leblond, J.-B., Devaux, J., 1993. Approximate models for ductile metals containing non-spherical voids. Case of axisymmetric prolate ellipsoidal cavities. J. Mech. Phys. Solids 41, 1723–1754. https://doi.org/10.1016/0022-5096(93)90029-F.

Gray III, G.T., 2000. Classic Split-Hopkinson pressure bar testing. In: Kuhn, H., Medlin, D. (Eds.), Mechanical Testing and Evaluation. ASM International.

Gurson, A.L., 1977. Continuum theory of ductile rupture by void nucleation and growth. I. Yield criteria and flow rules for porous ductile media. Trans. ASME.Ser. H, J. Eng. Mater. Technol., Trans. ASME, H, J. Eng. Mater. Technol. 99, 2–15.

Harding, J., Wood, E.O., Campbell, J.D., 1960. Tensile testing of materials at impact rates of strain. J. Mech. Eng. Sci. 2, 88–96.

Jones, I.P., Hutchinson, W.B., 1981. Stress-state dependence of slip in titanium-6Al-4V and other H.C.P. metals. Acta Metall. 29. https://doi.org/10.1016/0001-6160(81)90049-3.

Kolsky, H., 1949. An investigation of the mechanical properties of materials at very high rates of loading. Proc. Phys. Soc. B 62, 676.

Lewis, J.L., Campbell, J.D., 1972. Development and use of a torsional hopkinson-bar apparatus. Exp. Mech. 12, 520–524.

Milewski, J.O., 2017. Additive manufacturing of metals: from fundamental technology to rocket nozzles, medical implants, and custom jewelry. Springer Series in Materials Science. Springer International Publishing.

Nahshon, K., Hutchinson, J.W., 2008. Modification of the Gurson model for shear failure. Eur. J. Mech. / A Solids, Eur. J. Mech. A, Solids 27, 1–17. https://doi.org/10.1016/j.euromechsol.2007.08.002.

Nielsen, K.L., Dahl, J., Tvergaard, V., 2012. Collapse and coalescence of spherical voids subject to intense shearing: studied in full 3D. Int. J. Fract. 177. https://doi.org/10.1007/s10704-012-9757-4.

Oh, Y., Zhou, C., Behdad, S., 2018. Part decomposition and assembly-based (Re) design for additive manufacturing: a review. Addit. Manuf. 22, 230–242. https://doi.org/10.1016/j.addma.2018.04.018.

Rittel, D., Lee, S., Ravichandran, G., 2002. A shear-compression specimen for large strain testing. Exp. Mech. 42. https://doi.org/10.1007/BF02411052.

Rotbaum, Y., Osovski, S., Rittel, D., 2015. Why does necking ignore notches in dynamic tension? J. Mech. Phys. Solids 78. https://doi.org/10.1016/j.jmps.2015.02.005.

Roth, C.C., Morgeneyer, T.F., Cheng, Yin, Helfen, L., Mohr, D., 2018. Ductile damage mechanism under shear-dominated loading: in-situ tomography experiments on dual phase steel and localization analysis. Int. J. Plast. 109. https://doi.org/10.1016/j.ijplas.2018.06.003.

Scheyvaerts, F., Onck, P.R., Tekoglu, C., Pardoen, T., 2011. The growth and coalescence of ellipsoidal voids in plane strain under combined shear and tension. J. Mech. Phys. Solids 59. https://doi.org/10.1016/j.jmps.2010.10.003.

Tabachnikova, E.D., Bengus, V.Z., Stolyarov, V.V., Raab, G.I., Valiev, R.Z., Csach, K., Miskuf, J., 2001. The contribution of grain boundary dislocations to the plastic deformation of nanostructured titanium from the SD-effect of the yield stress. Mater. Sci. Eng. A (Structural Mater. Prop. Microstruct. Process 309–310. https://doi.org/10.1016/S0921-5093(00)01669-5.

Townsend, A., Senin, N., Blunt, L., Leach, R.K., Taylor, J.S., 2016. Surface texture metrology for metal additive manufacturing: a review. Precis. Eng. 46. https://doi.org/10.1016/j.precisioneng.2016.06.001.

Tvergaard, V., 2009. Behaviour of voids in a shear field. Int. J. Fract. 158. https://doi.org/10.1007/s10704-009-9364-1.

Tvergaard, V., Needleman, A., 1984. Analysis of the cup-cone fracture in a round tensile bar. Acta Metall. 32. https://doi.org/10.1016/0001-6160(84)90213-X.

Vrancken, B., Thijs, L., Kruth, J.-P., Van Humbeeck, J., 2012. Heat treatment of Ti6Al4V produced by selective laser melting: microstructure and mechanical properties. J. Alloys Compd. 541, 177–185. https://doi.org/10.1016/j.jallcom.2012.07.022.

Wang, X., Xu, S., Zhou, S., Xu, W., Leary, M., Choong, P., Qian, M., Brandt, M., Xie, Y.M., 2016. Topological design and additive manufacturing of porous metals for bone scaffolds and orthopaedic implants: a review. Biomaterials 83, 127–141. https://doi.org/10.1016/j.biomaterials.2016.01.012.

Weck, A., Wilkinson, D.S., 2008. Experimental investigation of void coalescence in metallic sheets containing laser drilled holes. Acta Mater. 56. https://doi.org/10.1016/j.actamat.2007.12.035.

Wilson-Heid, A.E., Novak, T.C., Beese, A.M., 2018. Characterization of the effects of internal pores on tensile properties of additively manufactured austenitic stainless steel 316L. Exp. Mech. https://doi.org/10.1007/s11340-018-00465-0.